



3-1-2001


Fractal Quasar Clouds

Mark Bottorff
University of Kentucky

Gary J. Ferland
University of Kentucky, gary@uky.edu

Right click to open a feedback form in a new tab to let us know how this document benefits you.

Follow this and additional works at: https://uknowledge.uky.edu/physastron_facpub

 Part of the [Astrophysics and Astronomy Commons](#), and the [Physics Commons](#)

Repository Citation

Bottorff, Mark and Ferland, Gary J., "Fractal Quasar Clouds" (2001). *Physics and Astronomy Faculty Publications*. 107.
https://uknowledge.uky.edu/physastron_facpub/107

This Article is brought to you for free and open access by the Physics and Astronomy at UKnowledge. It has been accepted for inclusion in Physics and Astronomy Faculty Publications by an authorized administrator of UKnowledge. For more information, please contact UKnowledge@lsv.uky.edu.

Fractal Quasar Clouds

Notes/Citation Information

Published in *The Astrophysical Journal*, v. 549, no. 1, p. 118-132.

© 2001. The American Astronomical Society. All rights reserved. Printed in the U.S.A.

The copyright holder has granted permission for posting the article here.

Digital Object Identifier (DOI)

<http://dx.doi.org/10.1086/319083>

FRACTAL QUASAR CLOUDS

MARK BOTTORFF AND GARY FERLAND

Department of Physics and Astronomy, University of Kentucky, Lexington, KY 40506

Received 2000 August 25; accepted 2000 October 20

ABSTRACT

This paper examines whether a fractal cloud geometry can reproduce the emission-line spectra of active galactic nuclei (AGNs). The nature of the emitting clouds is unknown, but many current models invoke various types of magnetohydrodynamic confinement. Recent studies have argued that a fractal distribution of clouds, in which subsets of clouds occur in self-similar hierarchies, is a consequence of such confinement. Whatever the confinement mechanism, fractal cloud geometries are found in nature and may be present in AGNs too. We first outline how a fractal geometry can apply at the center of a luminous quasar. Scaling laws are derived that establish the number of hierarchies, typical sizes, column densities, and densities. Photoionization simulations are used to predict the integrated spectrum from the ensemble. Direct comparison with observations establishes all model parameters so that the final predictions are fully constrained. Theory suggests that denser clouds might form in regions of higher turbulence and that larger turbulence results in a wider dispersion of physical gas densities. An increase in turbulence is expected deeper within the gravitational potential of the black hole, resulting in a density gradient. We mimic this density gradient by employing two sets of clouds with identical fractal structuring but different densities. The low-density clouds have a lower column density and large covering factor similar to the warm absorber. The high-density clouds have high column density and smaller covering factor similar to the broad-line region (BLR). A fractal geometry can simultaneously reproduce the covering factor, density, column density, BLR emission-line strengths, and BLR line ratios as inferred from observation. Absorption properties of the model are consistent with the integrated line-of-sight column density as determined from observations of X-ray absorption, and when scaled to a Seyfert galaxy, the model is consistent with the number of multiple UV absorption components observed in them. Rough estimates show that about one in 100 of the galaxies that harbor a supermassive black hole will show activity, assuming that material needs to be within its EUV continuum emitting radius for activity to occur. This is close to the observationally determined duty cycle. Stochastic feeding of the central engine of fractal cloud distribution of material may therefore account for continuum variations and long-term activity. The total cloud mass is much larger than that measured in ionized gas alone since the clouds are mutually self-shielding.

galaxies: ISM — quasars: emission lines — quasars: general — radiation mechanisms: thermal

1. INTRODUCTION

The broad-line region (BLR) of quasars and other active galactic nuclei (AGNs) are unresolved, and so their nature cannot be directly determined. Many ideas have been presented, including magnetically confined blobs (Rees 1987), winds above an accretion disk (Blandford & Payne 1982), continuum radiation driven winds (Mathews 1986), the disk itself (Collin-Souffrin 1987), tails behind ablating stars (Mathews 1983; Netzer & Alexander 1994), or filaments similar to those in the Crab Nebula (Davidson & Netzer 1979). No ab initio theory for the origin of these clouds is now possible, so a semiempirical approach is taken, often arguing by analogy with geometries encountered elsewhere in nature. The approach taken in most work is to devise a scenario for the presence of thermal matter, then compute the emitted spectrum, and finally compare this with observations to see whether conflicts arise.

In this paper we investigate whether fractal cloud distributions might describe the gas distribution in the center of a massive active galaxy. Observations of clouds in the interstellar medium (ISM) of our Galaxy (Elmegreen 1997; Elmegreen & Falgarone 1996; Heithausen et al. 1998) show that gas clusters in a fractal geometry extending over to 9 orders of magnitude in mass.

Theoretical work has argued that fractal clustering is a natural consequence of MHD turbulence. Numerical ex-

periments simulating the propagation of MHD waves through a gas show that clouds form and dissipate over a few dynamical crossing times (Elmegreen 1999; Mac Low & Ossenkopf 2000). Merging turbulent flows create temporary regions of enhanced density (clouds). Because clouds are constantly forming or dissipating, they are always present, removing the need for a confinement mechanism to maintain them. The numerical experiments further show that, contrary to expectation, higher levels of MHD-caused microturbulence produce structures with higher gas particle density. Structures with lower gas particle density, however, can also exist in the same environment.

Rees (1987) argued that BLR clouds are confined by a magnetic field in energy equipartition, and Bottorff & Ferland (2000) argued that MHD waves would result and could explain why line profiles are observed to be so smooth. The theory described above would argue that a fractal geometry must then result. In any case it is interesting to see whether a fractal geometry can reproduce the observed AGN spectrum.

Here we apply the fractal structure observed in the ISM but with length scales and gas densities appropriate for the BLR and the inner part of the narrow-line region (NLR) in AGNs. The choice of fractal geometry means that, from the largest to the smallest scales, clustering forms structures within structures that are self-similar. Thus, if any two

structures are compared, the substructures in each will appear similar, even if the two structures have different sizes. The self-similar structure is repeated, at ever smaller scales, to the point that each BLR cloud is a collection of overlapping constant density clumps. These smallest clumps we will call “cloud elements,” and for model simplicity the cloud elements are assumed to be spherical.

Several criteria must be satisfied for the model to be consistent with observations. (1) It should reproduce the observed BLR line intensity ratios and line equivalent widths. (2) The column density of individual BLR cloud elements should be of the order of $N_{\text{BLR}} \sim 10^{23} \text{ cm}^{-2}$ (Davidson & Netzer 1979). (3) Since the observed EW of the Ly α line is about 10% of that produced for full coverage of the continuum source, the ensemble should have a covering fraction (the fraction of the sky covered by BLR clouds, as seen by the continuum source) of about 10% (Peterson 1997). (4) The geometry should be spatially extended to account for observed range in BLR line variability. (5) Low-density clouds need to cover about 50% of the sky to be consistent with the statistics of warm absorbing (WA) gas in AGNs (Reynolds 1997). (6) The cumulative column density of the low-density clouds should be of the order of $N_{\text{WA}} = 10^{21.5} \text{ cm}^{-2}$ (Reynolds 1997; George et al. 1998).

In § 2 we describe the geometric details of a fractal distribution of BLR clouds. First, the basics of fractal clustering are reviewed. To be definite and to provide a visual example, a specific fractal distribution is illustrated and discussed. The average covering fraction of a fractal cloud distribution is shown to be a linearly increasing function of the integrated radius. The relative radius at which the covering fraction is 10% determines the relative extent of the BLR in the fractal. An estimate of the degree of cloud-to-cloud obscuration is made.

In § 3 general formulae describing the number, size, column density, and mass of individual fractal clouds are given. An absolute scale is set, following a discussion of the quasar continuum. If the continuum is known, then the size of the BLR and length scales for the substructures in the fractal distribution are in turn set. The general formulae are rewritten in terms of two parameters: (1) the volume-filling factor and (2) a geometric factor that describes the relative scale in a fractal structure. A method for estimating the covering factor is discussed, but its lengthy derivation is diverted to an appendix. The parameters are constrained by observation of WA gas in AGNs. This reduces the solution to only one free parameter, the volume-filling factor. Setting one more constraint, namely, that the column density (N [cm^{-2}]) of a BLR cloud element be of the order of $\log(N) = 23.0$, fixes a solution with no unconstrained free parameters. We note that in this model, a cloud element is the smallest structural unit of the fractal but the most important for reprocessing the AGN continuum into BLR emission lines. We will see, however, that the cloud elements strongly cluster together into larger, more distinct structures. To avoid confusion, we will always refer to the larger, more distinct structures as “clouds” and the smaller structures as “cloud elements.”

In § 4 the emission-line properties of the fractal BLR model are calculated and compared with observations. The emission-line spectrum produced by clouds with a cumulative covering fraction that is a linear function of spherical radius (a constant differential covering fraction) and a cumulative BLR covering factor of 0.1 are calculated. We

find that most of the bright observed lines or line blends are within a factor of 2 of observation if the gas particle density of the cloud elements in the BLR are $\sim 10^{10} \text{ cm}^{-3}$, reinforcing the assumption of the BLR gas particle density in §§ 2 and 3. In § 5 we discuss the plausibility of such a model as a description of gas within a few parsecs of the AGN continuum engine. Finally, our results are summarized in § 6.

2. FRACTAL FUNDAMENTALS

The fractal structure that is applied in this paper is purely a geometric model. It specifies, in a relative way, how structures of one length scale are related to another in terms of number, size, and proximity to one another. While there are indications, in both observation and simulation (Elmegreen & Falgarone 1996; Elmegreen 1997, 1999), that the physical mechanism that causes fractal structure is MHD turbulence, the physical mechanism that produces the fractal structure is left as an open question. As a result, the fractal model does not ab initio specify physical characteristics of the clouds such as their density, size (and therefore the resulting column density), or the extent of their distribution (e.g., the size of the BLR region). These must be constrained by observation, which we do in later sections.

The structure of a fractal is defined by three dimensionless parameters: the geometric factor ($L > 1.0$), the multiplicity (N), and the maximum hierarchy (H). The geometric factor L describes the relative size of the largest substructure within a structure. For example, if a structure has size ΔX , the largest substructure within it will have size ΔXL^{-1} . The multiplicity N defines the number of substructures of size ΔXL^{-1} in a structure of size ΔX . The values L and N are conveniently related to one another by the fractal dimension (D) defined by

$$D = \frac{\log(N)}{\log(L)}. \quad (1)$$

The value of D allows us to eliminate N by replacing it with L^D . Elmegreen & Falgarone (1996) found that the mean value of D for the ISM is $D \approx 2.3$, and we adopt this value. The maximum hierarchy H defines how many levels (hierarchies) of substructures there are from the largest scale to the smallest scale. Thus,

$$L^H = \frac{R_{\text{max}}}{S}, \quad (2)$$

where R_{max} is the characteristic maximum radius of the fractal distribution and S is the radius of a single cloud element.

Between R_{max} and S the size of a structure h hierarchies larger than S (or alternatively $H - h$ hierarchies smaller than R_{max}) is given by

$$R(h) = SL^h, \quad (3)$$

where h ranges from 0 to H . Each structure contains N substructures randomly distributed within it, and each substructure contains N sub-substructures randomly distributed within them, until at the smallest substructure ($h = 1$) there are N cloud elements of size S . The total number of cloud elements is therefore N^H (or alternatively L^{DH}), and the total number of cloud elements within any substructure of hierarchy h is L^{Dh} .

The cloud elements are not uniformly spread over the volume of the BLR, so their mean number density depends

on the hierarchy h . Following Elmegreen (1997), the mean number density $n_s(h)$ of cloud elements in a structure of size $R(h)$ is

$$n_s(h) = \frac{3}{4\pi S^3} L^{(D-3)h}. \quad (4)$$

Note that at the smallest scale $n_s(0) = 1/(4/3\pi S^3)$, corresponding to one cloud element per unit volume of cloud element. Further note that if $D < 3.0$ then the number density of cloud elements decreases with increasing structure size.

A simple fractal is illustrated in Figure 1a. The figure shows the two-dimensional projection onto a plane of a fractal structure in three-dimensional space. The fractal shown has $D = 2.3$, $L \approx 3.05$, and $H = 3$. In the figure the smallest spheres represent cloud elements. The value of L is chosen because the number of substructures per structure is an integer ($L^D \approx 3.05^{2.3} \approx 13$), making it easy to illustrate and describe. In addition, it is close to a fiducially chosen value of 3.0 and an observationally constrained value close to 3.2 (see below). In principle, however, L^D need not be an integer. In such a case L^D represents the average number of structures per substructure.

The sphere in Figure 1a labeled 1 is a factor of 3.05 larger than a cloud element and contains 13 cloud elements with centers randomly distributed within the sphere. Likewise, the sphere labeled 2 is a factor of 3.05^2 times larger than a cloud element and contains the centers of 13 spheres of the size labeled 1 randomly distributed within it. Finally the largest sphere (labeled 3) is 3.05^3 times larger than a cloud element and contains 13 spheres of the size labeled 2 randomly distributed within it. The total number of cloud elements in the fractal structure is therefore $13^3 = 2197$.

Using $D = 2.3$ and $L \approx 3.05$, equation (4) becomes $n_s(h) = 2.18^{-h}/(3/4\pi S^3)$. Thus, the cloud element density decreases with increasing h . Equation (4) somewhat overpredicts the density of cloud elements at high values of h because it does not take into account the fact that some cloud elements can be outside of a substructure. For example, the sphere labeled 2 has cloud elements within it that exist outside of the sphere labeled 3. The equation, however, is exact for $h = 1$.

We note that the cloud element density is so high within the sphere labeled 1 that cloud elements strongly overlap one another in volume and projected area. This is not the case, however, for the spheres labeled 2 and 3. Cloud elements in these overlap less, and their overall structure appears clumpy with relatively more empty space between clumps.

Small-scale clustering and obscuration are more clearly illustrated in Figure 1b. The figure shows a slice through the center of the fractal structure in Figure 1a. The thickness of the slice is taken to be one cloud element diameter. The cloud elements in the slice produce varying degrees of cloud-to-cloud obscuration in the structure. Three examples of obscuration are shown. The dotted-line pairs show columns through the cloud having cross section $4S^2$. Cloud elements with centers that fall within the volumes are shown as filled circles. Along the column labeled i there are four cloud elements. If there were a continuum source to the right of the figure, the cloud element farthest to the right (provided it is optically thick) would obscure the continuum from the others. The column density through this path is therefore roughly 4 times the column density of a single cloud element. Because the elements are not connected, however, they should not be considered as part of a single cloud. Along the column labeled ii there are only two cloud

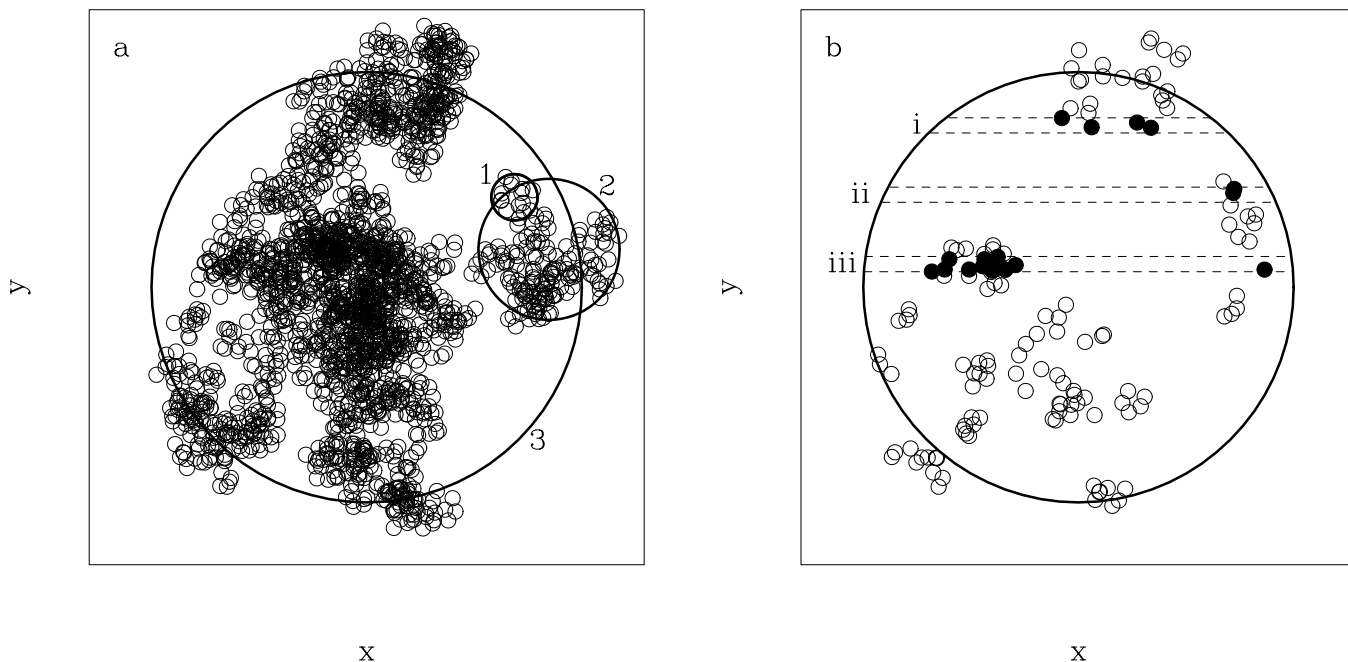


FIG. 1.—(a) Orthogonal projection of a randomly chosen three-dimensional fractal structure of hierarchy 3 on a plane. The circles labeled 1, 2, and 3 show the relative sizes of successively larger structural elements. In this figure each labeled circle is 3.05 times larger than the previous one. If this were a small part of an AGN fractal cloud distribution, the smallest circles would correspond to “cloud elements.” In this model there are about 13 cloud elements tightly packed within the circle labeled 1. Because of the tight packing, we define a “cloud” to be a cluster of cloud elements one hierarchy larger than a cloud element. (b) Thin slice through the center of the $H = 3$ fractal. Three line-of-sight paths (*dashed-line pairs*) show varying degrees of obscuration from cloud elements (*filled circles*). Note that the most dense regions are roughly the same size as circle 1 in (a).

elements. These strongly overlap, but there are also cloud elements just above and below the pair. The column labeled *ii* must therefore cut the edge of a larger local structure, so the two elements together are not representative of a cloud. The column labeled *iii*, however, cuts through the center of a distinct structure of closely packed cloud elements. Other structures like it are also visible in the figure and are roughly L times the diameter of a cloud element.

The preceding discussion emphasizes the fact that the clustering of cloud elements is greatest at the level $h = 1$. The volumes of individual cloud elements, within an $h = 1$ substructure, overlap so much that their individuality loses meaning. We therefore define a “cloud” to be a structure one hierarchy higher than that of a cloud element. Thus, a cloud has characteristic radius SL and mass $(4/3)\pi S^3 n \mu L^D$, where n is the hydrogen gas particle density of a cloud element and μ is the mean atomic weight of the gas (here we take $\mu \approx 1.4$ amu).

Important cloud properties, from the standpoint of photoionization considerations, are the cloud particle density and column density. The average column density, along an arbitrary center line through a cloud structure, is L^D times the expected column contribution of a single cloud element along the line. Thus, we have

$$\langle N_{\text{cloud}} \rangle = L^D \int_0^S n 2\sqrt{S^2 - r^2} \frac{4\pi r \sqrt{(SL)^2 - r^2}}{(4/3)\pi(SL)^3} dr, \quad (5)$$

where $4\pi r[(SL)^2 - r^2]^{1/2} dr / (4/3)\pi(SL)^3$ is the probability that a cloud element is within a perpendicular distance r to $r + dr$ of the center line through the cloud and $n 2(S^2 - r^2)^{1/2}$ is the column density contribution of a cloud element to the center line. Equation (5) may be rewritten as

$$\langle N_{\text{cloud}} \rangle = 2(SL)nI(L), \quad (6)$$

where $2(SL)n$ is the column density through the center of a sphere of radius SL with uniform density n and

$$I(L) = 3L^{D-3} \int_0^1 \sqrt{1-w^2} \sqrt{1-\left(\frac{w}{L}\right)^2} w dw \quad (7)$$

is the correction for the fractal structure. The integration is straightforward but tedious. A value of $L \approx 3.0$, for example, gives $I(L) \approx 0.45$, a little less than half that if the cloud were a solid sphere.

In equations (5) and (6) the expression n is the density of a cloud element. This simple model, however, allows the cloud elements to interpenetrate, producing a local density enhancement within a cloud. This will be important for photoionization considerations only if overlap between cloud elements within a cloud results in a density enhancement of a factor of about 2 or more over a significant volume of the ionized part of a cloud. We estimate the probability of such an event by calculating the probability that, in an isolated cloud, any given cloud element is overlapped a distance S or less by one or more other cloud elements. At the center of the cloud this probability is given by

$$P(R < S) = (L^D - 1) \left[\frac{(4/3)\pi S^3}{(4/3)\pi(LS)^3} \right] = (L^D - 1)L^{-3}. \quad (8)$$

When $L \approx 3.0$ and $D = 2.3$, the probability of a density enhancement of a factor of 2 or more is 43% at the center of a cloud. The probability is largest near the center of the

cloud because a cloud element can have any part of its volume occupied by another cloud element. A cloud element with its center near the edge of the cloud, however, can only be occupied in the part of its volume interior to the sphere of radius LS . Thus, the probability of overlap at the cloud boundary is less. When corrected for the probability gradient within a cloud, the probability is only 0.19 at the cloud edge where continuum reprocessing is expected to occur. We therefore neglect density enhancements in the photoionization calculations presented in § 4.

2.1. Two Fractals

Fractal structure is caused by turbulence, possibly produced by MHD waves, and higher turbulence results in higher average particle density (Elmegreen 1999). Physically, there would be higher levels of turbulence closer to the central object if turbulence scales with depth into the potential well, as occurs for many forms of MHD turbulence (Rees 1987; Bottorff & Ferland 2000). What is expected then is that at each radial distance R (or if the luminosity of the central engine is fixed, at each hydrogen ionizing flux Φ) there will be a chaotic mix of clouds of different densities. The gray area in Figure 2 shows a schematic diagram of the range of density in the $\log(n)$ -versus- $\log(\Phi)$ plane due to turbulence in equipartition with gravity. At high values of $\log(\Phi)$, corresponding to small values of R , turbulence is large, the result is the mean density, and the range of possible cloud densities is large. At small values of $\log(\Phi)$, corresponding to large values of R , turbulence is small, the result is the mean density, and the range of possible densities is small.

Clouds illuminated by the continuum at each value of $\log(\Phi)$ contribute to the emission lines of the quasar. The

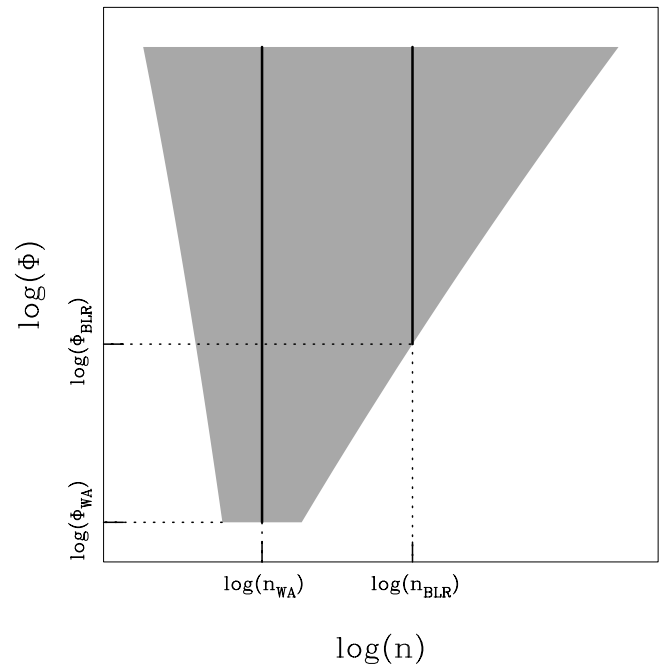


FIG. 2.—Qualitative schematic diagram of the range of gas density as a function of flux (gray area). Deep in the gravitational potential (toward higher flux) the turbulence is high, resulting in a broad range in gas density. Farther out (toward lower flux) turbulence is less and results in a smaller range in gas density. In addition, the mean gas density for high levels of turbulence is expected to be higher than the mean gas density at low levels of turbulence. The superimposed black vertical lines show the simplified density distribution used in our model.

total emission-line flux is a result integrating over the number distribution of illuminated clouds in the $\log(n)$ -versus- $\log(\Phi)$ plane, the surface area of each cloud, and the cloud emissivity, which is subject to strong selection effects (Baldwin et al. 1995). Unfortunately, a detailed theory linking turbulence, structure size, and density for compressible fluids does not yet exist. Such integration is therefore not yet possible without approximation. In addition, we wish to avoid invoking a particular dynamical scenario (e.g., inflow, outflow, rotation, etc.) since this is now unknown and we want to focus on the effects of fractal structure. We therefore invoke a simple model involving two sets of clouds with identical fractal structure but different densities. A high-density fractal is embedded within a low-density fractal so that the mean density and the range of density decrease, in stepwise fashion, with increasing radius. The density distribution for our simple model is illustrated in Figure 2 by the two vertical solid lines and is meant to mimic crudely the gray area. Inside the BLR there are two densities, a high-density component and a low-density component, denoted as n_{BLR} and n_{WA} , respectively. (See below for an explanation of the nomenclature.) Outside the BLR only the low-density component continues. The boundary of the BLR at flux Φ_{BLR} is set by the dust sublimation boundary, and the outer boundary of the low-density component is at a distance corresponding to the outer boundary of the fractal (see § 3 below for details).

Observationally, the central regions of an AGN have at least two components: the BLR, high-density gas seen in emission, and the WA, gas only detected by its absorption. The WA is likely to have lower density, which would account for its lower emissivity. It is therefore natural to attempt to associate our two-fractal model with the WA and the BLR. The low-density fractal is given a density of $n \sim 10^7 \text{ cm}^{-3}$ and is required to have a covering fraction of about 0.5 to be consistent with the current statistics of WA gas in AGNs (Reynolds 1997). The high-density fractal, corresponding to BLR clouds, is given a density of $n \sim 10^{10} \text{ cm}^{-3}$ and is required to have a covering fraction of 0.1 to be consistent with the energy output of BLR emission lines relative to the continuum (Peterson 1997). The geometry is investigated to see if a fractal cloud distribution can reproduce observations of quasars.

2.2. The Covering Factor

We envision an AGN continuum source placed at the center of a fractal cloud distribution. The continuum illuminates cloud elements at the leading edge of BLR clouds causing them to produce emission-line radiation. The distance of a cloud from the continuum source, the gas density, the column density, and the abundances determines the emergent emission-line flux from a cloud. The total luminosity of a line, however, depends on the covering factor of the cloud ensemble.

The cumulative cloud covering factor $f(R)$ at radius R is given by integrating the fraction of sky covered by each cloud element. Accounting for possible cloud-cloud overlap, along any line of sight, this is given by

$$f(R) \approx \int_0^R n_{\text{eff}} \frac{\pi S^2}{4\pi r^2} 4\pi r^2 dr. \quad (9)$$

Here n_{eff} is the effective cloud element number density including correction for cloud overlap along the line of sight; $\pi S^2/4\pi r^2$ is approximately the fraction of sky covered

by a cloud element of radius S at a distance r from the continuum source, as seen from the continuum source; and $4\pi r^2 dr$ is a differential volume element. Implicit in this approximation is that $\pi S^2/4\pi r^2 \ll 1.0$.

Any particular fractal distribution is clumpy, but the probability distribution of clumps is random, and therefore averaged over the ensemble of possible fractal distributions for a given L , H , and D , n_{eff} is constant out to R_{max} . We may therefore write the covering fraction formula as

$$f(R) \approx n_{\text{eff}} \pi S^2 R. \quad (10)$$

Thus, $f(R)$ (or rather its ensemble average) is a linear function of R , meaning that the differential covering fraction ($df/dR = n_{\text{eff}} \pi S^2$) is a constant. The linear covering fraction function implies that the maximum extent of the WA fractal must be about 5 times that of the BLR to account for the difference between the covering fractions; therefore, we have

$$R_{\text{max}} = 5.0 R_{\text{BLR}}. \quad (11)$$

Since a given L and H can yield a covering fraction slightly larger or smaller than 0.5, a small correction is added to the coefficient 5.0 in equation (11) to ensure always that the BLR covering fraction is 0.1. For all of our calculations the correction is at most only a few percent.

The total covering fraction $f(R_{\text{max}})$ may be rewritten as

$$\begin{aligned} f(R_{\text{max}}) &\approx \frac{n_{\text{eff}} \pi S^2}{4\pi} \frac{4\pi}{3} R_{\text{max}}^3 \\ &\times \frac{\int_0^{R_{\text{max}}} (1/R^2) 4\pi R^2 dR}{(4\pi/3) R_{\text{max}}^3} = \frac{N_{\text{eff}}}{4} S^2 \frac{3.0}{R_{\text{max}}^2} \quad (12) \\ &= \frac{3}{4} N_{\text{eff}} \left(\frac{S}{R_{\text{max}}} \right)^2 = \frac{3}{4} N_{\text{eff}} L^{-2H}, \quad (13) \end{aligned}$$

where N_{eff} is the effective number of clouds (the effective number density times the volume of the BLR) and $3.0/R_{\text{max}}^2$ is the volume-weighted value of $1/R^2$ over the fractal.

The derivation of a direct method for approximating $f(R_{\text{max}})$ as a scale-free function of L and H is presented in Appendix A. [Note: a graph of $f(R_{\text{max}})$ for $L = 3.0$ as a function of H appears in Appendix A in Fig. 5b.] Here, however, we utilize equations (12) and (13) to calculate the fraction of clouds directly exposed to the continuum. This is given by solving equations (12) and (13) for N_{eff} and dividing by the total number of cloud elements (L^{DH}), yielding

$$\frac{N_{\text{eff}}}{L^{DH}} = \frac{4}{3} f(R_{\text{max}}) L^{(2-D)H}. \quad (14)$$

For $f(R_{\text{max}}) = 0.5$ we have $N_{\text{eff}}/L^{DH} = 0.1(20/3)L^{(2-D)H}$. To illustrate, using easy to work with values, close to the ones obtained when a physical scale is set to the fractal distribution (see § 3), we choose $L = 3.0$, $H = 11$, and $D = 2.3$. The resulting ratio with these values is 0.018. Thus, in this case, only one out of 56 cloud elements is directly exposed to the continuum. The rest are partially shielded by intervening low-density, optically thin (see below) clouds.

High-density clouds are optically thick (see below), and therefore significant obscuration is to be expected. This is now estimated for the BLR portion of the fractal structure. The volume-weighted average solid angle of sky covered by

a BLR cloud element is

$$\begin{aligned}\Omega &\approx \frac{\pi S^2}{(R_{\text{BLR}}/\sqrt{3})^2} = 3\pi \left(\frac{S}{R_{\text{BLR}}}\right)^2 \\ &= 3\pi \left(\frac{S}{R_{\text{max}}/5}\right)^2 = 75\pi L^{-2H},\end{aligned}\quad (15)$$

and the number of obscuring clouds is therefore given by $N_{\text{eff, BLR}} \Omega = 4\pi(0.1)$. Solving for $N_{\text{eff, BLR}}$ gives $N_{\text{eff, BLR}} = 0.1(4/75)L^{2H}$. Since the number of BLR clouds is $L^{DH}/125$, the fraction of BLR cloud elements (and therefore clouds) not obscured is $125N_{\text{eff, BLR}}/L^{DH} = 0.1(20/3)L^{H(2-D)}$. This is identical to the fraction not obscured in the whole fractal structure. Apparently, the decrease in number is made up for by the decrease in the required total covering factor and the increase in the solid angle subtended by a BLR cloud element.

The shielding of many cloud elements by a few is made possible by the clustering of structures in a fractal. Figures 3a and 3b show an orthogonal projection onto a plane of the upper and lower half of a fractal with $L = 3.05$ and $H = 4$. The figure shows the strong clustering trend. If we were to imagine that this were instead a fractal with $H = 11$ (as in our fiducial values above), then each of the smallest circles in the figure would actually contain $L^{D(11-4)} \approx 6.3 \times 10^7$ cloud elements or, by the above definition of a cloud, $L^{D(11-4)}/L^D \approx 4.8 \times 10^6$ clouds. To put Figures 3a and 3b into perspective, the larger dot-dashed circle has radius R_{max} and represents the outer boundary of the inner part of the NLR. The inner solid circle has radius $R_{\text{max}}/5.0$ and represents the outer boundary of the BLR.

Our shielding estimates thus far have been presumptive. We can, however, estimate the average relative number of cloud elements obscured along a line of sight directly by using the derivation in Appendix A. This is calculated by

dividing the number of cloud elements by the number of obscuring cloud elements in the largest substructure (of size R_{max}/L). An example is shown in Figure 5a in Appendix A. The crosses in the figure show a graph of the area of cloud elements per unit area of substructure as a function of hierarchy h for a fractal with $H = 11$ (and $L = 3.0$) given as $A(11, h)/\pi(SL^h)^2$. Here the function $A(11, h)$ is a special case of the general function $A(H, H - i)$, derived in Appendix A, which directly integrates the projected area of cloud elements within a substructure of hierarchy $h = H - i$. To illustrate, consider the structure associated with the circle labeled 2 in Figure 1a. This is a substructure of hierarchy $h = 2$ in an $H = 3$ fractal. If the areas of the cloud elements (*small circles*) interior to the circle labeled 2 are shaded, then $A(3, 2)$ is the shaded area. $A(3, 2)/\pi(SL^2)^2$ is then the relative area per unit area of structure.

Returning to Figure 5a, we see that $A(11, 10)/\pi(SL^{10})^2 \approx 0.46$, which means that, 10 levels above the smallest scale (and one level below the largest scale), the cloud elements shadow 46% of a circle of radius R_{max}/L .

All cloud elements, regardless of whether they are shielding or shielded, lie within this projected area. The (equivalent) number of shielding elements is $A(11, 10)/\pi S^2 = 1.6 \times 10^9$, the total number of cloud elements in the structure is thus $(L^D)^{10} \approx 9.4 \times 10^{10}$, and the ratio of unshielded cloud elements to shielding ones is $(9.4 \times 10^{10} - 1.6 \times 10^9)/1.6 \times 10^9 \approx 58$. Compared with the value of ~ 56 in the above estimate and given the approximations involved, the result obtained through direct methods is consistent with the previous estimate. The important point here is not so much the precise value, since that depends on the geometry chosen for the cloud elements. Moreover, approximations have been made in both the estimate and the direct calculation. Rather, the important point is that in a fractal structure shielding of many cloud elements by a few is possible.

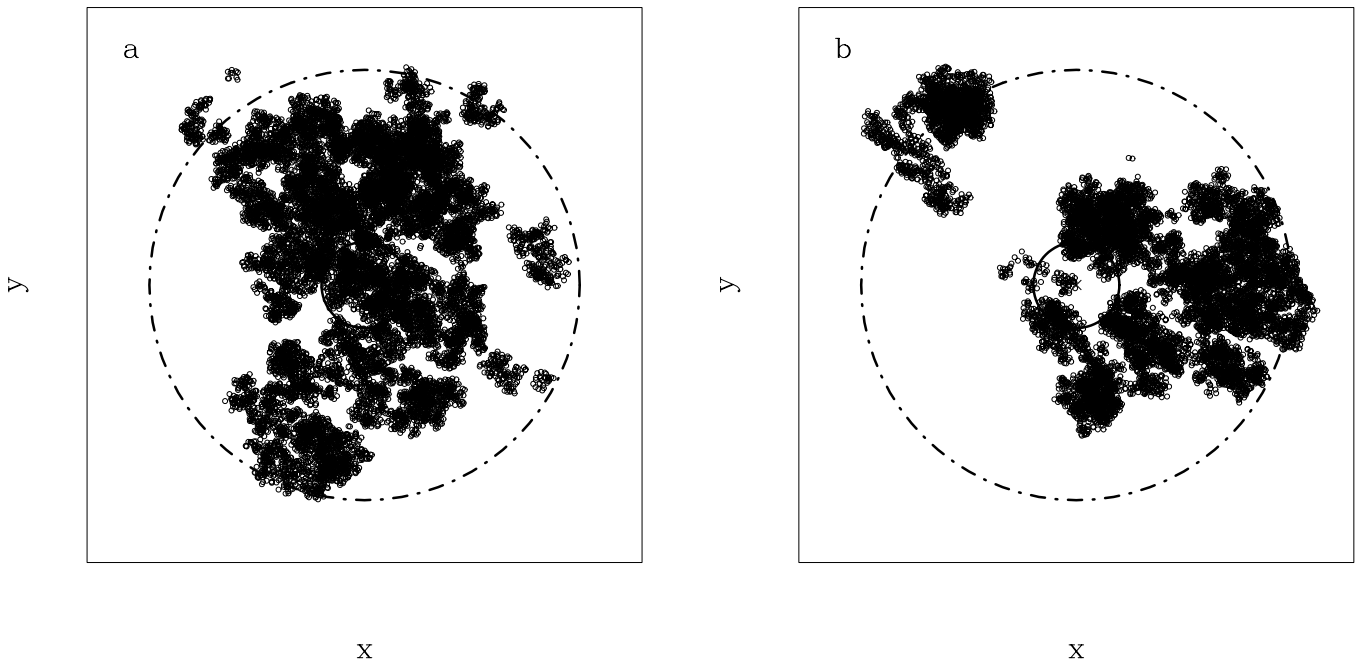


FIG. 3.—(a) Orthogonal projection of the upper half of a fractal of hierarchy 4 onto a plane. If this figure were representative of a fractal distribution of clouds near an AGN, then each smallest circle in the figure would contain additional hierarchies of structure and millions of clouds. The dot-dashed circle represents the extent of low-density material that we associate with the WA, and the solid circle represents the extent of the BLR clouds. (b) The same as (a), except that the lower half of the fractal is shown.

The average number of line-of-sight clouds shielded per shielding cloud can be estimated in a similar way as the cloud elements. The (equivalent) number of shielding clouds is given by $A(11, 10)/A(11, 1) \approx 2.5 \times 10^8$, and the total number of clouds in the structure is $L^{D(10^{-1})} \approx 7.5 \times 10^9$. The ratio of shielded clouds to unshielded clouds is thus $(7.5 \times 10^9 - 2.5 \times 10^8)/2.5 \times 10^8 \approx 29$. Consequences of shielding are discussed in § 5.

3. SETTING A PHYSICAL SCALE TO FRACTAL BLR CLOUDS

The fractal parameters L and H may be related to the more physical but still dimensionless variable ϵ , the volume-filling factor of the clouds. We distinguish ϵ from the volume-filling factor of the emitting gas, which we denote by ϵ_{emit} ; ϵ_{emit} is a small fraction of ϵ due to shielding or ionization fronts. Its value is estimated later in this section. Following Elmegreen (1997), the relative volume between clouds is given approximately by

$$\frac{V_{\text{empty}}}{V_{\text{total}}} \approx 1 - \left(\frac{L^D}{L^3}\right)^H. \quad (16)$$

The volume-filling fraction $\epsilon = V_{\text{full}}/V_{\text{empty}}$ is thus

$$\epsilon \approx L^{D(3-H)}. \quad (17)$$

Solving for H in terms of L and ϵ gives

$$H = \frac{\log(\epsilon)}{(D-3)\log(L)}, \quad (18)$$

and therefore

$$L^{-H} = \epsilon^{1/(3-D)}. \quad (19)$$

Recalling that the number of cloud elements is L^{DH} and that there are L^D cloud elements per cloud, the number of clouds, Σ , in the fractal structure is

$$\Sigma = \epsilon^{D/(D-3)} L^{-D}. \quad (20)$$

Since $S = R_{\text{max}} L^{-H}$, the radius of a cloud element is $S = R_{\text{max}} \epsilon^{1/(3-D)}$, so the radius of a cloud is

$$R_{\text{cloud}} = R_{\text{max}} \epsilon^{1/(3-D)} L, \quad (21)$$

and the column density through the center of the cloud is

$$\langle N_{\text{cloud}} \rangle = 2R_{\text{max}} \epsilon^{1/(3-D)} LI(L)n. \quad (22)$$

The mass of a cloud, M_{cloud} , is L^D times the mass of one cloud element, thus

$$M_{\text{cloud}} = \mu n \frac{4\pi}{3} R_{\text{max}}^3 \epsilon^{(3/3-D)} L^D. \quad (23)$$

The result is that all important physical quantities are expressed in terms of four quantities: two free parameters, L and ϵ ; R_{max} , which is fixed by R_{BLR} and the WA covering fraction; and n , which will be set by the requirements of the relative strengths of observed quasar emission lines.

In this section we take the density of BLR cloud elements to be $\sim 10^{10} \text{ cm}^{-3}$ in anticipation of the optimal density that we find for emission lines (see § 4 below). Physically, the outer boundary of the BLR is set at the radius where emission lines are suppressed as a result of the onset of dust formation. This occurs at a hydrogen ionizing number flux $\Phi = 10^{18} \text{ cm}^{-2} \text{ s}^{-1}$ (Netzer & Laor 1993). If the bolometric continuum luminosity L_b is given, then R_{BLR} can be deter-

mined. With $L_b = L_{46} \times 10^{46} \text{ ergs s}^{-1}$, the flux Φ at distance $R = R_{18} \times 10^{18} \text{ cm}$ from the continuum source is

$$\Phi = \frac{L_b}{4\pi R^2 \langle E \rangle} f_H = 4.87 \times 10^{19} \frac{L_{46}}{R_{18}^2 \langle E_{\text{eV}} \rangle} (\text{cm}^{-2} \text{ s}^{-1}), \quad (24)$$

where $\langle E_{\text{eV}} \rangle$ is the mean ionizing photon energy in eV and f_H is the fraction of ionizing photons above 1 ryd.

For the continuum that we use (see § 4 for further details), the fraction of the luminosity in ionizing photons is $f_H = 0.658$ and the mean energy of photons above 13.6 eV is $\langle E_{\text{eV}} \rangle = 44.23 \text{ eV}$. Substituting $\Phi = 10^{18} \text{ cm}^{-2} \text{ s}^{-1}$ and solving for the radius gives

$$\begin{aligned} R_{\text{BLR}} &= 6.98 \times 10^{18} \sqrt{\frac{L_{46} f_H}{\langle E_{\text{eV}} \rangle}} (\text{cm}) \\ &= 8.51 \times 10^{17} \sqrt{L_{46}} (\text{cm}). \end{aligned} \quad (25)$$

The radius of the fractal is 5 times this, so

$$R_{\text{max}} = 4.26 \times 10^{18} \sqrt{L_{46}} (\text{cm}). \quad (26)$$

The establishment of a distance scale for R_{max} allows us to scale the other quantities. First, we have

$$S = 8.22 \times 10^{12} \sqrt{L_{46}} \epsilon_{-4}^{10/7} (\text{cm}), \quad (27)$$

where $\epsilon_{-4} = \epsilon/10^{-4}$ and

$$R_{\text{cloud}} = 8.22 \times 10^{12} \sqrt{L_{46}} \epsilon_{-4}^{10/7} L (\text{cm}). \quad (28)$$

As discussed in § 1, the fractal cloud model is assumed to have two populations of clouds. If the clouds are in overall virial equilibrium, then cloud density will tend to increase with decreasing radius. In MHD simulations the range in cloud density also increases. The net effect is that clouds closer to the central source tend to have a higher micro-turbulence, to be denser, and to have a wider range of densities. Clouds with particle density 10^7 cm^{-3} are found throughout the fractal structure. Clouds exterior to R_{BLR} form the inner part of the NLR. Clouds inside R_{BLR} may be remnants of dispersed high-density BLR clouds or precursors to converging flows. All of the low-density material is a potential candidate for a warm absorber. Therefore, we will refer to low-density clouds as WA clouds. The cloud column densities for the two cloud types are thus

$$\langle N_{\text{BLR}} \rangle = 1.64 \times 10^{23} \sqrt{L_{46}} \epsilon_{-4}^{10/7} LI(L)n_{10} (\text{cm}^{-2}) \quad (29)$$

and

$$\langle N_{\text{WA}} \rangle = 1.64 \times 10^{20} \sqrt{L_{46}} \epsilon_{-4}^{10/7} LI(L)n_7 (\text{cm}^{-2}), \quad (30)$$

where $n_{10} = n/10^{10} \text{ (cm}^{-3}\text{)}$ and $n_7 = n/10^7 \text{ (cm}^{-3}\text{)}$. Likewise, the cloud masses are

$$M_{\text{BLR}} = 2.72 \times 10^{-8} (\sqrt{L_{46}})^3 \epsilon_{-4}^{30/7} L^{2.3} n_{10} (M_{\odot}) \quad (31)$$

and

$$M_{\text{WA}} = 2.72 \times 10^{-11} (\sqrt{L_{46}})^3 \epsilon_{-4}^{30/7} L^{2.3} n_7 (M_{\odot}). \quad (32)$$

Since the BLR is 5 times more compact than the fractal, the number of BLR clouds is 5^3 times less than the number of WA clouds. The number of WA clouds is

$$\Sigma_{\text{WA}} = 1.39 \times 10^{13} \epsilon_{-4}^{-23/7} L^{-2.3}, \quad (33)$$

and so the number of BLR clouds is

$$\Sigma_{\text{BLR}} = 1.11 \times 10^{11} \epsilon_{-4}^{-23/7} L^{-2.3}. \quad (34)$$

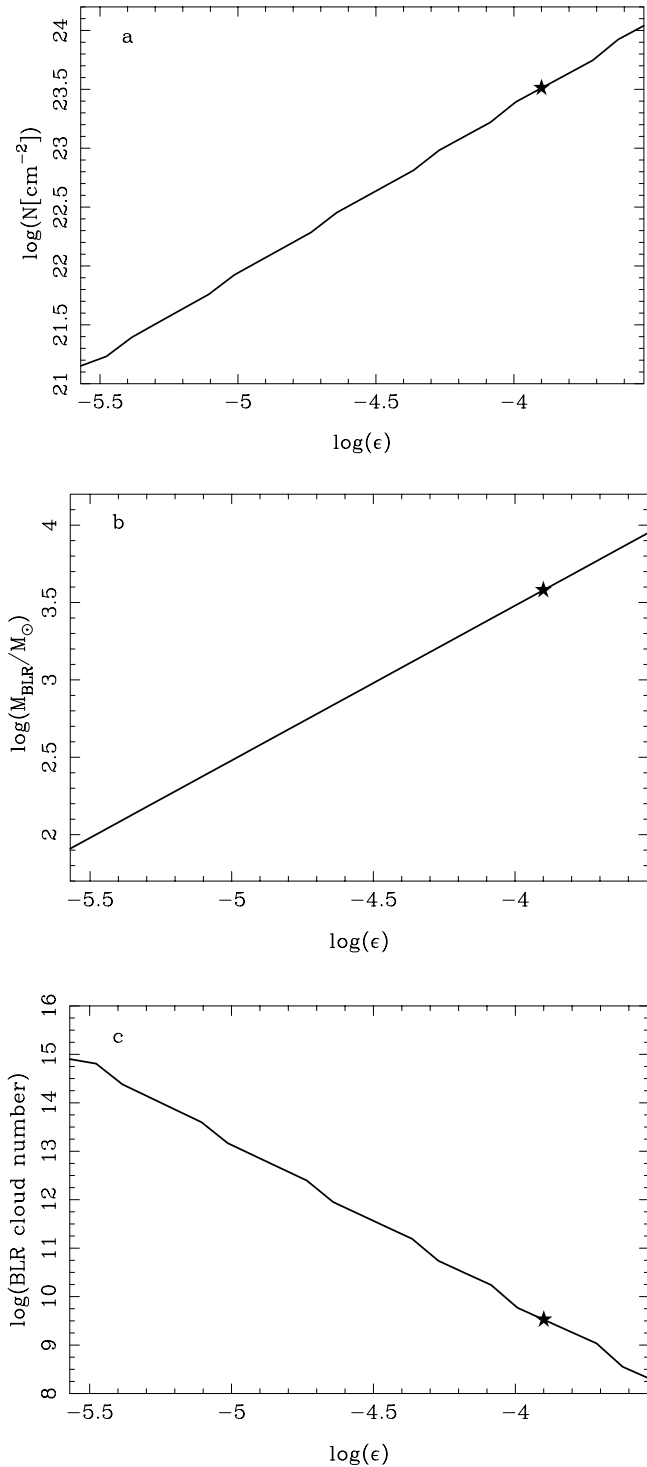


FIG. 4.—(a) Plot of column density, (b) total BLR mass, and (c) BLR cloud number as a function of volume-filling factor ϵ . The star graph marker shows the values when the column density of a cloud element is 10^{23} cm^{-2} .

The total BLR mass is $M_{\text{BLR}}(\text{total}) = \Sigma_{\text{BLR}} M_{\text{BLR}}$. Likewise, the total WA mass is $M_{\text{WA}}(\text{total}) = \Sigma_{\text{WA}} M_{\text{WA}}$. Thus,

$$M_{\text{BLR}}(\text{total}) = 3.02 \times 10^3 \epsilon_{-4} (\sqrt{L_{46}})^3 n_{10} (M_{\odot}) \quad (35)$$

and

$$M_{\text{WA}}(\text{total}) = 3.77 \times 10^2 \epsilon_{-4} (\sqrt{L_{46}})^3 n_7 (M_{\odot}). \quad (36)$$

For the purpose of analyzing variability, we also calculate the number of high-velocity BLR clouds. Suppose that the local velocity field is given by $v^2 \sim 1/R$. Since $\Phi \sim 1/R^2$, we have $v \sim \Phi^{1/4}$. We normalize the velocity so that it is 300 km s^{-1} when $\Phi = 10^{18} \text{ cm}^{-2} \text{ s}^{-1}$. This scales the velocity field so that it is typical of narrow line velocity widths at the flux where BLR lines are suppressed from dust formation (Netzer & Laor 1993). Since quasar emission lines have FWZM of the order of 10^3 – 10^4 km s^{-1} (Netzer 1990), we define the high-velocity (and/or high-turbulence) clouds to have $v > 2500 \text{ km s}^{-1}$. This gives $\Phi > 10^{21.68} \text{ cm}^{-2} \text{ s}^{-1}$. Since $R \propto \Phi^{-1/2}$, the radius, inside which $v > 2500 \text{ km s}^{-1}$, is 69.4 times smaller than R_{BLR} , so the number of BLR clouds with $v > 2500 \text{ km s}^{-1}$ ($\Sigma_{\text{BLR},2500}$) is 69.4^3 times less than the total number of BLR clouds. The number of high-velocity clouds is

$$\Sigma_{\text{BLR},2500} = 3.32 \times 10^5 \epsilon_{-4}^{-23/7} L^{-2.3}. \quad (37)$$

In terms of ϵ the fraction of BLR clouds not obscured (i.e., illuminated) is $0.1(20/3)\epsilon^{(D-2)/(3-D)} \approx 1.29 \times 10^{-2} \epsilon_{-4}^{3/7}$. Thus, the number of illuminated BLR clouds is

$$\Sigma_{i,\text{BLR}} = 1.43 \times 10^9 \epsilon_{-4}^{-23/7} L^{-2.3}, \quad (38)$$

and the number of illuminated BLR clouds with $v > 2500 \text{ km s}^{-1}$ is

$$\Sigma_{i,\text{BLR},2500} = 4.16 \times 10^3 \epsilon_{-4}^{-23/7} L^{-2.3}. \quad (39)$$

$\Sigma_{i,\text{BLR}}$ may be used to estimate the emission volume-filling factor, ϵ_{emit} . The thickness of the ionization front, D , is given by

$$D \approx 10^{23} \frac{\Phi}{cn^2} (\text{cm}) \quad (40)$$

(Ferland 1999), where n is the gas particle density and c is the speed of light. For the value of D we use $n = n_{10} \times 10^{10} \text{ cm}^{-3}$ and the value of Φ at $R = R_{\text{BLR}}/3^{1/2}$. Since $\Phi \propto R^{-2}$ and the flux is $10^{18} \text{ cm}^{-2} \text{ s}^{-1}$ at R_{BLR} , then $\Phi = 3 \times 10^{18} \text{ cm}^{-2} \text{ s}^{-1}$. Substitution of these quantities gives $D \approx 10^{11} n_{10}^{-2} \text{ cm}$. To estimate ϵ_{emit} , we first calculate the volume of the part of the spherical cloud element between the surface that faces the continuum and an identical spherical surface displaced a distance D toward the cloud element interior. This is given by $J(D, S) = \pi S^3 (D/S)$ for $D/S \ll 1$. The volume is then multiplied by the number of illuminated cloud elements ($L^3 \Sigma_{i,\text{BLR}}$) and divided by the volume of the BLR, $(4/3)\pi R_{\text{BLR}}^3$, to give

$$\epsilon_{\text{emit}} \approx 1.18 \times 10^{-8} \frac{n_{10}}{\sqrt{L_{46}}} \epsilon_{-4}^{-3/7}. \quad (41)$$

The choice of ϵ and L controls the number, size, column density, mass, and the emission volume-filling factor. Possible values for ϵ and L are determined by requiring the covering fraction (derived in Appendix A as a function of H and L) to have a value in the range 0.50 ± 0.05 . In order to search the two-dimensional parameter space of L and ϵ , we replaced L in terms of H and ϵ via

$$L = \epsilon^{1/(D-3)H}, \quad (42)$$

making the covering fraction a function of H and ϵ . This transformation is convenient because H is an integer and L is readily found from H and ϵ . The integer H was allowed to range from 2 to 50, and $\log(\epsilon)$ was allowed to range

TABLE 1
PROPERTIES OF A SAMPLE FRACTAL AGN MODEL^a

Category	Property	Symbol	Value
Geometry	Fractal dimension	D	2.3
	Geometric factor	L	3.2098
	Substructures per hierarchy	L^D	14.62
	Number of hierarchies	H	11
Length (cm)	log (number of smallest structures)	$\log(L^D)$	11.65
	log (BLR radius)	$\log(R_{\text{BLR}})$	17.93 ^b
	log (maximum radius)	$\log(R_{\text{max}})$	18.64 ^c
	log (cloud radius)	$\log(R_{\text{cloud}})$	13.57 ^d
Column density (cm ⁻²)	log (cloud element radius)	$\log(S)$	13.07 ^e
	log (BLR cloud column density)	$\log(N_{\text{BLR}})$	23.51 ^f
	log (WA cloud column density)	$\log(N_{\text{WA}})$	20.51 ^g
Number	log (BLR cloud number)	$\log(\Sigma_{\text{BLR}})$	9.52
	log (BLR cloud number, $v < 2500$ km s ⁻¹)	$\log(\Sigma_{\text{BLR},2500})$	4.00 ^h
	log (WA cloud number)	$\log(\Sigma_{\text{WA}})$	11.14 ⁱ
	log (mass BLR cloud)	$\log(M_{\text{cloud}})$	-5.94
Mass (M_{\odot})	log (mass BLR)	$\log(M_{\text{BLR}})$	3.58
	log (mass BLR for $v > 2500$ km s ⁻¹)	$\log(M_{\text{BLR},2500})$	-1.94
	log (mass WA)	$\log(M_{\text{WA}})$	2.70
	log (mass BLR cloud)	$\log(M_{\text{cloud}})$	-5.94
Covering fraction	BLR covering fraction	f_{BLR}	0.10
	WA covering fraction	f_{WA}	0.51
Filling factor	log (BLR filling factor)	ϵ_{BLR}	-3.90
	log (emission filling factor)	ϵ_{WA}	-6.09 ^j

^a Indicated by a star in Fig. 4.

^b Value obtained from $R_{\text{BLR}} = 8.51 \times 10^{17}(L_{46})^{1/2}$ (cm) and $L_{46} = 1.0$.

^c $R_{\text{max}} = R_{\text{BLR}} 10^{0.71}$.

^d $R_{\text{cloud}} = R_{\text{max}} L^{-H+1}$.

^e $S = R_{\text{max}} L^{-H}$.

^f $N_{\text{BLR}} = 2nR_{\text{cloud}}$, where $n = 10^{10}$ cm⁻³.

^g $N_{\text{WA}} = 2nR_{\text{cloud}}$, where $n = 10^7$ cm⁻³.

^h Velocity normalized so that $\log(v/300 \text{ km s}^{-1}) = 0.25 \log(\Phi/10^{18} \text{ cm}^{-2} \text{ s}^{-1})$.

ⁱ $\Sigma_{\text{WA}} = L^{D(H-1)}$.

^j Assumes that the thickness of the ionization layer is 10^{11} cm.

between -7.0 and -2.0 in steps of 0.093 . Values of H and $\log(\epsilon)$ that made the covering fraction function (see Appendix A) satisfy the above constraint were filtered out for further analysis.

Figures 4a, 4b, and 4c show the resulting cloud column density, total BLR mass, and total BLR cloud number as functions of ϵ . The slight wiggles in the cloud column density and the cloud number are due to the corrections that maintain an average BLR covering fraction of 0.1 . Given the explorative nature of our calculations, however, further fine-tuning is not justified. Of the set of solutions obtained, the mean covering fraction is 0.50 ± 0.02 , and the mean geometric factor is $L = 3.16 \pm 0.10$. Of particular interest is the solution at $\log(\epsilon) = -3.90$ because this solution has a BLR cloud element column density $\log[N_{\text{BLR}} (\text{cm}^{-2})] = 23.0$ corresponding to column densities inferred in the BLR (Davidson & Netzer 1979). The solution is marked by a star in the graphs of Figure 4 and is summarized numerically, in greater detail, in Table 1. In § 5 we discuss this solution in the context of the emission-line calculations presented below in § 4.

4. EMISSION-LINE PROPERTIES OF A FRACTAL BLR CLOUD DISTRIBUTION

In the previous section the physical and geometric properties of a fractal AGN model were established. The observed emission-line spectrum is predicted in this section. Calculations of the spectrum of constant density clouds, having an integrated covering fraction linear with radius,

were carried out using CLOUDY (Version 95.00). The maximum integrated covering fraction was normalized to 0.1 at an ionizing flux of $10^{18} \text{ cm}^{-2} \text{ s}^{-1}$. BLR cloud densities were allowed to vary from 10^7 to 10^{14} cm^{-3} , while the column density (N) was normalized so that $N = 10^{23.5} (n/10^{10} \text{ cm}^{-3}) (\text{cm}^{-2})$, where n is the particle density. With this normalization the cloud size remains the same for all densities. This grid is similar to those given in Korista et al. (1997), which contains further details.

The clouds are illuminated by the continuum given in Korista et al. (1997). The shape is given by

$$f_{\nu} = v^{\alpha_{\text{UV}}} \exp\left(-\frac{h\nu}{kT_{\text{BB}}}\right) \exp\left(-\frac{kT_{\text{IR}}}{h\nu}\right) + av^{\alpha_{\text{X}}}, \quad (43)$$

where a is chosen so that

$$\frac{f_{\nu}(2 \text{ keV})}{f_{\nu}(2500 \text{ \AA})} = 403.3^{\alpha_{\text{OX}}}. \quad (44)$$

The specific parameters are $\alpha_{\text{UV}} = -0.50$, $T_{\text{BB}} = 10^{6.0} \text{ K}$, $kT_{\text{IR}} = 0.01 \text{ ryd}$, $\alpha_{\text{X}} = -1.0$, and $\alpha_{\text{OX}} = -1.40$. The full continuum between 912.02 cm and 100.01 MeV is considered. The inner radius is set where the flux is $10^{24} \text{ cm}^{-2} \text{ s}^{-1}$. Above this flux emission lines are suppressed by thermalization. In absolute measure this limits the inner radius to about $1.05 \times 10^{15}(L_{46})^{1/2} \text{ cm}$.

Photoionization predictions are listed in Table 2. The table shows 11 bright emission-line blends relative to the Ly α line and the equivalent width of Ly α . The first column

TABLE 2
LINE STRENGTH RELATIVE TO $\text{Ly}\alpha$: OBSERVATION AND FRACTAL MODEL

Emission-Line Blend	Zheng	Baldwin	10^{7a}	10^8	10^9	10^{10}	10^{11}	10^{12}	10^{13}	10^{14}
O III $\lambda 835$ + O II $\lambda 834$	0.014	...	0.008	0.007	0.006	0.006	0.005	0.005	0.007	0.007
C III $\lambda 977$ + Ly γ $\lambda 973$	0.009	0.007–0.20	0.011	0.014	0.019	0.036	0.042	0.038	0.036	0.027
N III $\lambda 990$	0.011	0.013	0.005	0.006	0.006	0.007	0.006	0.006	0.009	0.007
O VI $\lambda 1032$ + O VI $\lambda 1037$ + Ly β $\lambda 1026$	0.190	0.068–0.69	0.333	0.445	0.322	0.106	0.040	0.027	0.022	0.026
N V $\lambda 1239$ + N V $\lambda 1243$	0.110	0.069–0.099	0.008	0.022	0.049	0.030	0.013	0.012	0.011	0.006
Si IV $\lambda 1394$ + Si IV $\lambda 1403$ + O IV $\lambda 1402$	0.075	0.022–0.50	0.010	0.018	0.045	0.076	0.051	0.035	0.033	0.017
C IV $\lambda 1548$ + C IV $\lambda 1551$	0.620	0.087–0.65	0.400	0.586	0.733	0.656	0.278	0.130	0.086	0.039
He II $\lambda 1640$ + O III $\lambda 1663$ + Al II $\lambda 1671$	0.068	0.013–0.14	0.128	0.122	0.128	0.136	0.097	0.126	0.237	0.303
C III $\lambda 1909$ + Si III $\lambda 1892$ + Al III $\lambda 1859$	0.163	0.076–0.74	0.033	0.054	0.099	0.153	0.118	0.044	0.029	0.022
Mg II $\lambda 2796$ + Mg II $\lambda 2804$	0.250	0.15–0.30 ^b	0.003	0.010	0.037	0.144	0.382	0.933	2.339	5.727
H β $\lambda 4861$	0.07–0.20 ^b	0.016	0.023	0.026	0.031	0.049	0.144	0.911	3.515
EW(Ly α)/1216	0.076	0.03–0.20	0.031	0.053	0.065	0.073	0.069	0.033	0.009	0.004

^a Density in units of cm^{-3} .

^b Ranges for observations are from Baldwin et al. 1995.

gives the line identification. The second column gives a list of observed values as derived from the mean quasar survey of Zheng et al. (1997). The third column gives the observed line blend ranges for a set of high signal-to-noise quasars (Baldwin et al. 1995). These two columns may be compared with the remaining columns of the table that show the model results for different densities. The equivalent width of Ly α that best matches the Zheng et al. (1997) value occurs at a density of 10^{10} cm^{-3} , for an integrated covering fraction of 0.1.

Table 3 compares the 10^{10} cm^{-3} model with observations in greater detail. The first column of Table 3 gives the emission-line blend. The second column shows the relative difference between the emission-line strengths of the mean quasar spectrum in Zheng et al. (1997) and the model. With the exception of the C III $\lambda 977$ + Ly γ $\lambda 973$ blend (where the model yields values 4 times what is observed) and the He II $\lambda 1640$ + O III $\lambda 1663$ + Al II $\lambda 1671$ blend (where the model yields values twice what is observed), the predicted emission-line strengths are within the dispersion of the mean quasar spectrum. The third column of Table 3 indicates whether the model falls within the observed range of the Baldwin et al. (1995) data. The model reproduces seven of the 10 lines. Of the remaining three ranges, one (Mg II $\lambda 2796$ + Mg II $\lambda 2804$) just misses the range. The fourth column of Table 3 indicates whether the model is within a

factor of 2 of the mean quasar spectrum and the ranges of the Baldwin et al. (1995) data. In all cases, except for the C III $\lambda 977$ + Ly γ $\lambda 973$ blend, the 10^{10} cm^{-3} model is within a factor of 2 compliance with observations. We judge this to be an adequate fit, given that no effort was made to fine-tune parameters such as the continuum shape or chemical composition to reproduce the spectrum.

5. DISCUSSION

5.1. The Observed Spectrum

The fractal model of the AGN environment produces a large family of possible solutions in a two-parameter phase space (L vs. H or equivalently ϵ vs. H). Fortunately, the family is constrained to one parameter, the volume-filling factor ϵ , by our requirement that the covering fraction of the fractal be of order 0.5. The cloud column density is a monotonic function of ϵ , so a solution where the column density of a BLR cloud element is equal to what is inferred from observation ($\sim 10^{23.0} \text{ cm}^{-2}$) is guaranteed. The strengths of BLR emission lines and their strength relative to Ly α , however, are not guaranteed. These depend on the differential covering factor, the cloud gas density, and the properties of the continuum. Nevertheless, for a reasonable choice of continuum, we find that BLR emission-line strengths are close (most within a factor of 2) to those

TABLE 3
FRACTAL MODEL AT 10^{10} cm^{-3} VERSUS OBSERVATION

Emission-Line Blend	(Zheng-Model)/Zheng	In the Baldwin Range?	Factor of 2 Compliance?
O III $\lambda 835$ + O II $\lambda 834$	0.57	...	Yes
C III $\lambda 977$ + Ly γ $\lambda 973$	-3.00	Yes	No (4 times larger)
N III $\lambda 990$	0.36	0.46 ^a	Yes
O VI $\lambda 1032$ + O VI $\lambda 1037$ + Ly β $\lambda 1026$	0.44	Yes	Yes
N V $\lambda 1239$ + N V $\lambda 1243$	0.73	No (low by 0.56)	Yes
Si IV $\lambda 1394$ + Si IV $\lambda 1403$ + O IV $\lambda 1402$	-0.01	Yes	Yes
C IV $\lambda 1548$ + C IV $\lambda 1551$	-0.06	Yes	Yes
He II $\lambda 1640$ + O III $\lambda 1663$ + Al II $\lambda 1671$	-1.00	Yes	Yes
C III $\lambda 1909$ + Si III $\lambda 1892$ + Al III $\lambda 1859$	0.06	Yes	Yes
Mg II $\lambda 2796$ + Mg II $\lambda 2804$	0.42	No (low by 0.04)	Yes
H β $\lambda 4861$	No (low by 0.56)	Yes
EW(Ly α)/1216	0.04	Yes	Yes

^a (Baldwin-Model)/Baldwin (range is a single entry in Table 1).

observed when the density is 10^{10} cm^{-3} . Though the cloud column density was normalized to $10^{23.5} \text{ cm}^{-2}$ when the density was 10^{10} cm^{-3} , the fact that the depth of the ionization front in the cloud (or rather the continuum facing cloud elements of a cloud) is of order $10^{22} n_{10}^{-1} \text{ cm}^{-2}$ implies that the clouds are radiation bounded for densities from $10^{9.25} \text{ cm}^{-3}$ to the maximum density of the calculations (10^{14} cm^{-3}). Thus, in this range of parameters, it is the gas density that predominantly determines the relative emission-line spectrum. The optimal density of 10^{10} cm^{-3} that we found is therefore not a result of fine-tuning the column density. We conclude that a fractal cloud distribution can reproduce observations of BLR quasar emission-line strengths for canonical values of the cloud column density.

5.2. The Warm Absorber

The low-density fractal, which was added to mimic a possible density-radius relationship, reproduces many of the observed properties of the warm absorber. If we take the density of these clouds to be $\sim 10^6\text{--}10^7 \text{ cm}^{-3}$, as inferred for WA clouds (Reynolds & Fabian 1995), and the expected number of absorbing clouds along the line of sight to be ~ 30 (§ 2, last paragraph), then the total integrated column density ranges from $N_{\text{WA}} \sim 10^{21}$ to 10^{22} cm^{-2} . This is consistent with WA column densities inferred from ASCA observations by Reynolds (1997) and George et al. (1998) for a variety of AGNs. The fractal model column densities are also consistent with the integrated column densities inferred for multicomponent UV absorbers detected in Seyfert 1 galaxies (Crenshaw & Kraemer 1999; Mathur, Elvis, & Wilkes 1999).

In these objects up to six distinct UV absorption components have been observed. The fractal cloud distribution predicts just this number. The number of clouds along the line of sight is proportional to the radial distance through the fractal structure, and in this model the maximum scale is proportional to $(L_b)^{1/2}$. Thus, by lowering the (average) luminosity, the number of line-of-sight clouds is lowered. In this paper we took $L_b \approx 10^{46} \text{ ergs s}^{-1}$. If we scale to the luminosity of a Seyfert galaxy, say NGC 5548 with $L_b \approx 10^{44.4} \text{ ergs s}^{-1}$, the number of clouds along the line of sight is reduced from 30 to roughly $30(10^{44.4}/10^{46})^{1/2} \approx 5$, which is consistent with observations. We point out, however, that randomly selected fractal structures and randomly chosen viewing angles will produce a wide range of line-of-sight cloud counts. Nevertheless, the fact that the predicted number of line-of-sight absorbers is within an order of magnitude of observations is encouraging.

5.2.1. Implications for Variability

A fractal structure is clumpy. There are regions dense with structure and regions void of structure. Many models of the central activity predict that the central black hole has a small duty cycle and is only luminous on occasions when accreting material is within a certain radius. This accretion radius can be taken as the radius of the region where the EUV originates, since this must be the radius of the accretion disk. We take this radius to be that given by observed line-continuum reverberation. We scale from the well-observed Seyfert galaxy NGC 5548, with EUV variability timescale of the order of 1 day (Marshall et al. 1997), to a quasar luminosity of $10^{46} \text{ ergs s}^{-1}$ by assuming, as we did above, that the radius scales as $(L_b)^{1/2}$. This gives an accretion radius of $R_{\text{accretion}} \sim 1.63 \times 10^{16} \text{ cm}$. The fraction of

quiescent galaxies is then given by the probability that material is *not* within $R_{\text{accretion}}$. We can estimate this probability by calculating the likelihood that a fractal structure of size $R_{\text{accretion}}$ lies a distance $R_{\text{accretion}}$ or more from the central black hole. To be specific, we consider the model outlined in Table 1 where $D = 2.3$, $H = 11$, and $L = 3.2098$. For this model $R_{\text{accretion}}$ is roughly six hierarchies larger than a cloud element or alternatively five hierarchies smaller than the maximum extent of the fractal. We therefore need to calculate the probability that in a fractal of hierarchy 11 there are zero substructures of hierarchy 6 within a distance $R_{\text{max}} L^{-5}$ (or alternatively a distance SL^6) of the continuum source. We symbolize this probability by $P_6^{11}(0)$. It is given iteratively via

$$P_6^l(0) = [L^{-3} P_6^{l-1}(0) + (1 - L^{-3})]^{L^D} \quad (l = 8, \dots, 11), \quad (45)$$

where

$$P_6^7(0) = (1 - L^{-3})^{L^D} \quad (46)$$

(eqs. [45] and [46] are derived for the case $L^D \in I$ in Appendix B). The chosen values of D , H , and L yield $P_6^{11}(0) = 0.99$. This result suggests that in the set of galaxies with a central supermassive black hole roughly 1% will have nuclear activity at any time. Our result is comparable to observation if we presume that every galaxy has a massive central object, in which case the percentage of galaxies observed to have nuclear activity is a little over 2% (see Table 3 of Woltjer 1990).

5.3. Accretion Duty Cycle

If we assume that the black hole accretes with an efficiency of ~ 0.1 (Blandford 1990), then a luminosity of $10^{46} \text{ ergs s}^{-1}$ corresponds to a mass accretion rate of about 10^{26} g s^{-1} (roughly $1.6 M_{\odot} \text{ yr}^{-1}$). Since a structure six hierarchies above a cloud element has mass $(L^D)^5 M_{\text{cloud}} \approx 1.5 \times 10^{33} \text{ g}$, the black hole will consume this structure in $1.5 \times 10^7 \text{ s}$, about half a year. Since AGNs are observed to be luminous much longer than this, material must be replenished. The fractal structure helps in this because of its clumpy structure. Thus, while the chances of finding material close to the continuum source are small (one in 100), the chance of finding additional material in the vicinity of the continuum source *if material is already present* is large. The time for local material to migrate to the region of the continuum source and replenish the fuel supply can be found by dividing the distance to the nearest neighboring structure of hierarchy 6, in a structure of hierarchy 7, by the magnitude of the turbulent velocity field, which we take to be of order 2000 km s^{-1} . The distance to the nearest neighbor is estimated by assuming that the structure of hierarchy 6 that is feeding the continuum is at the center of a structure of hierarchy 7. At increasing radius r the chances of finding another one of the $L^D - 1$ remaining structures of hierarchy 6 increase in proportion to the volume. The probability is unity when $1 = (L^D - 1)[r/R(7)]^3$, where $R(7)$ is the size of a structure of hierarchy 7. For this model $R(7) = L^D S \approx 4 \times 10^{16} \text{ cm}$. Solving for r gives $r \approx 10^{16} \text{ cm}$, giving a timescale of $5 \times 10^7 \text{ s}$. This is the same order of magnitude as the feeding timescale. Therefore, quasi-continuous feeding of clumps into the black hole can occur. The observed continuum variability on the timescale of a year may therefore be due to erratic feeding rates of material clumped in a fractal structure.

At an accretion rate of $1.6 M_{\odot} \text{ yr}^{-1}$ the entire fractal structure will be depleted in about 2500 yr unless the central parsec is resupplied from without. One possibility is that the fractal structure continues to larger scales until it merges with a molecular torus. Another possibility is that the central parsec is relatively void of gas but occasionally cloud fragments perturbed off the torus migrate into the region causing lighting up the central engine to produce a quasar. The latter case is more consistent with our model because the line-of-sight column densities and cloud counts are consistent with observations when the fractal structure terminates at $10^{18.64} \text{ cm}$ (1.4 pc). If the fractal structure continued, the integrated line-of-sight column density of clouds would be far higher than observed.

5.4. Kinetic Luminosity

To this point we have focused on the geometric aspects of a fractal cloud model and have not discussed dynamics. Whatever the dynamical mechanism involved, the most important point to be aware of is that the fractal structure hides most of its mass. A dynamical mechanism that requires *the entire* fractal to participate in a systematic motion must be able to account for the resulting kinetic luminosity of the shielded mass. For example, suppose the BLR mass in our model has an average systematic velocity of 10^4 km s^{-1} . The kinetic luminosity is then $L_k = 1.5M_{\text{BLR}} V^3 R_{\text{BLR}}^{-1} \approx 1.25 \times 10^{46} \text{ ergs s}^{-1}$. This is comparable to the luminosity of a typical quasar. Therefore, unless only part of the fractal is being driven, radiation pressure may be energetically insufficient.

6. CONCLUSIONS

We find that a fractal description of the distribution of material in the central parsec of an AGN is capable of explaining a wide variety of phenomena associated with observations of AGNs. The chief successes are the following:

1. The BLR spectrum is consistent with formation in a chaotic mix of clouds with various properties, along with the selection effects introduced by the atomic physics

(Baldwin et al. 1995). A fractal geometry can result from large-scale chaos and may be inevitable if the region is in magnetic equipartition.

2. The observed emission-line spectrum is consistent with formation in a fractal geometry. This geometry is simultaneously consistent with the covering factor, density, column density, BLR emission-line strengths, and BLR line ratios, as deduced from observations of BLR emission lines.

3. A considerable fraction of the BLR clouds are predicted to lie in shadows cast by interior clusters of clouds. As a result, the total mass is predicted to be much larger than the ionized mass detected by emission lines. This has obvious consequences on the energetics.

4. Absorption properties of the fractal model are found to be consistent with the integrated line-of-sight column density as determined from observations of X-ray absorption. When the model is scaled to a Seyfert galaxy, we find that the number of line-of-sight clouds is consistent with the number of multiple UV absorption components observed in them.

5. Rough estimates show that about one in 100 of the galaxies that harbor a supermassive black hole will show activity, assuming that material needs to be present within its EUV continuum emitting radius for activity to occur. This is close to the observationally determined duty cycle.

6. Stochastic feeding of the central engine of fractal cloud distribution of material may account for continuum variations and long-term activity.

7. A fractal cloud distribution may or may not be part of additional dynamical processes such as in a disk, a line-driven wind, or a systematic MHD flow. If it does participate, care must be taken to include the kinetic luminosity of all the fractal mass and turbulent energy.

This work was supported by the NSF through grant AST-0071180 and by NAS through its LTSA program. We thank Kirk Korista, Jack Baldwin, and Bruce Elmegreen for a thorough reading of the manuscript and many helpful comments.

APPENDIX A

A DIRECT METHOD OF ESTIMATING THE COVERING FRACTION

In this appendix an approximate method for determining $f(R_{\text{max}})$ as a scale-free function of H and L is derived. We start at a structure one hierarchy larger than individual BLR cloud elements (i.e., at level $H - 1$, or equivalently, at the scale of a single cloud). We assume for this derivation that $SL/R \ll 1.0$ so light from the continuum source passes through the structure along nearly parallel rays. Cloud elements on the continuum side of the structure obscure cloud elements on the far side of the structure.

The differential area of the cloud elements, dA_c , per unit area of cross section, dA , projected along parallel rays on an imaginary plane behind the structure including cloud element-to-cloud element obscuration is given by

$$\frac{dA_c}{dA} = 1 - \exp(-n_c \pi S^2 \Delta X), \quad (\text{A1})$$

where n_c , the cloud element number density not including obscuration, is given by $n_c = L^D/[4/3\pi(LS)^3]$ and X is the distance through the structure along a ray centered on dA . The total projected cloud area due to a spherical structure of size LS is thus

$$A_c(H, 1) = \int_0^{SL} 2\pi r [1 - \exp(n_c \pi S^2 2X)] dr = \int_0^{SL} 2\pi X [1 - \exp(n_c \pi S^2 2X)] dX, \quad (\text{A2})$$

where $X^2 + r^2 = (SL)^2$ and the argument $(H, 1)$ has been added to emphasize that this calculation applies to a substructure, in a fractal of hierarchy H , one hierarchy larger than a cloud element. Integration gives

$$A_c(H, 1) = \pi(SL)^2 + \frac{2\pi(SL)^2}{(2\pi n_c S^3 L)^2} [(2\pi n_c S^3 L + 1) \exp(-2\pi n_c S^3 L) - 1]. \quad (\text{A3})$$

The effective number of cloud elements in the structure is $A_c(H, 1)$ divided by the cross-sectional area of a single cloud element. We therefore have

$$N_{\text{eff}}(H, 1) = \frac{A_c(H, 1)}{\pi S^2}. \quad (\text{A4})$$

We note that this equation is approximate because it does not account for additional area of cloud elements that project area onto the plane outside of the projected sphere of radius LS . This contribution to the projected area is expected to be comparatively small, however (visually compare, in Fig. 1a, the projected areas of cloud elements outside of, but still associated with, the structures corresponding to spheres 1, 2, and 3 to the projected area of the cloud elements within them), so we neglect it in our calculations.

The above method is now applied to structure with scale SL^2 . Since there are L^D substructures of size SL in a structure of size SL^2 , the density of the substructures two levels less than the maximum hierarchy H is $n_s(2) = L^D/[4/3\pi(SL^2)^3]$ and the effective cross-sectional area of a substructure is $A_c(H, 1)$. Thus, $A_c(H, 2)$ is obtained by replacing n_c and πS^2 with $n_s(2)$ and $A_c(H, 1)$, respectively, in equation (A2). This gives

$$A_c(H, 2) = \pi(SL^2)^2 + \frac{2\pi(SL^2)^2}{Q(H, 2)^2} \{[Q(H, 2) + 1] \exp[-Q(H, 2)] - 1\}, \quad (\text{A5})$$

where

$$Q(H, 2) = 2n_s(2)A_c(H, 1)SL^2. \quad (\text{A6})$$

In general,

$$A_c(H, i) = \pi(SL^i)^2 \left(1 + \frac{2\{[Q(i) + 1] \exp[-Q(i)] - 1\}}{Q(i)^2} \right), \quad (\text{A7})$$

where

$$Q(H, i) = 2n_s(i)A_c(H, i-1)SL^i \quad (\text{A8})$$

and

$$n_s(i) = \frac{L^D}{(4/3)\pi(SL^i)^3}. \quad (\text{A9})$$

An example of the progression of $A_c(H, i)/\pi(SL^i)^2$ for $i = 0-11$, $L = 3.0$, and $L = 3.2098$ is shown in Figure 5a. The effective cloud number i hierarchies larger than a cloud element is thus

$$N_{\text{eff}}(H, i) = \frac{A_c(H, i)}{\pi S^2}. \quad (\text{A10})$$

Equation (A10) assumes that the continuum source is on one side of the fractal substructure under consideration. It cannot be utilized to calculate $N_{\text{eff}}(H, H)$ and thereby determine $f(R_{\text{max}})$ because, in this last case, the continuum source is embedded within the fractal. Instead, $N_{\text{eff}}(H, H)$ is approximated by assuming that there is no significant cloud-to-cloud obscuration between structures of hierarchy $H - 1$ because a line of sight from the continuum traverses only half of the fractal. This means that $N_{\text{eff}}(H, H)$ is given by $N_{\text{eff}}(H, H - 1)$ times the number of substructures having $N_{\text{eff}}(H, H - 1)$, so we have $N_{\text{eff}}(H, H) \approx N_{\text{eff}}(H, H - 1)L^D$. Since $R_{\text{max}} = SL^H$, we have

$$f(R_{\text{max}}) \approx \frac{3}{4} N_{\text{eff}}(H, H - 1) L^D \left(\frac{S}{R_{\text{max}}} \right)^2 = \frac{3}{4} N_{\text{eff}}(H, H - 1) L^{D-2H}. \quad (\text{A11})$$

This shows that since D is fixed the covering fraction is a function of two free parameters (L and H) and (as expected) is scale free.

Values of $f(R_{\text{max}})$ corresponding to fractals with $L = 3.0$ (the fiducially chosen value; see § 2) and $L = 3.2098$ (the physically constrained value; see § 3) are shown in Figure 5b. Because $N_{\text{eff}}(H, H)$ does not take into account structure overlap of the largest substructures, the calculation slightly overpredicts the covering fraction. The values at $H = 0$, where the error will be the least accurate, are too large by 4%–7%. In the figure, the horizontal solid line is at a covering fraction of 0.5 and the dashed lines indicate a $\pm 10\%$ range. Note that for L near 3.0 there are about seven or eight possible solutions within this range. Further physical constraints and restrictions of the covering factor (see the main text for details) narrow the set possible solutions.

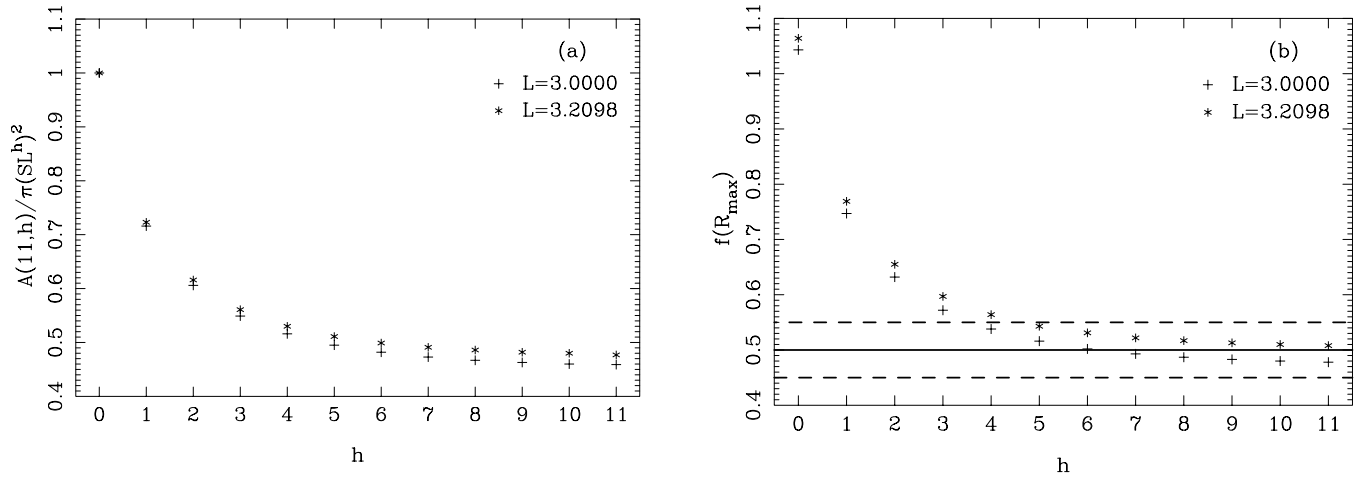


FIG. 5.—(a) Projected area of various substructures of hierarchy h in a fractal of hierarchy 11. The decreasing values illustrate that clouds “hide” behind other clouds so there is less and less available surface-projected surface area as h gets larger. (b) Covering fraction as a function of hierarchy. Note that for $L = 3.20898$ and $h = 11$ the covering fraction is close to 0.5 (solid line). Dashed lines show 10% ranges.

APPENDIX B

DERIVATION OF AN ESTIMATE FOR $P_6^{11}(0)$

We wish to calculate the probability that there will be zero structures of hierarchy 6 (or smaller) within a distance of SL^6 of the center of the EUV region that resides in a fractal of hierarchy 11. We consider the case in which the number of substructures in a structure L^D is an integer. The derivation is an approximation because it assumes that all substructures associated with a structure lie within the characteristic radius of the structure. Figure 1a shows that this is mostly the case but not always. A small portion of substructure associated with each structure (the circles labeled 1, 2, and 3) lies outside the characteristic structure radius. Making this approximation introduces the error that a structure with hierarchy h becomes denser with substructures of hierarchy $h - 2$ or less than it would otherwise be. If the EUV region lies inside such a structure, the probability of *not* finding material in it is decreased. On the other hand, with this same approximation, if the EUV region is just outside the characteristic radius of a structure, the probability of *not* finding material in it is enhanced. The approximation therefore makes small, somewhat offsetting errors. In a similar approximation we assume that the EUV region either is contained entirely within a larger structure or is outside of it. This avoids the mathematically messy and geometry-dependent details of calculating probabilities when the EUV region lies near the boundary of a structure. As in the case of the earlier assumption, this approximation introduces small, partially offsetting errors. The probability of *not* finding material in the EUV region is decreased if it is within the characteristic radius of the structure and enhanced if it is without.

Suppose the EUV region is within a structure of hierarchy 7. The probability p_6^7 that any one of the L^D substructures of hierarchy 6 is a distance greater than SL^6 from the center of the EUV region is given by

$$p_6^7 = 1 - \frac{(4/3)\pi(SL^6)^3}{(4/3)\pi(SL^7)^3} = 1 - \frac{1}{L^3}, \quad (\text{B1})$$

and the probability, $P_6^7(0)$, that none of the substructures of hierarchy 6 are closer than SL^6 to the center of the EUV region is

$$P_6^7(0) = (1 - L^{-3})^{L^D} \quad (\text{B2})$$

(this is eq. [46] of the text). An expression for $P_6^8(0)$, the probability that when the EUV region is interior to a structure of hierarchy 8 there are no structures of hierarchy 6 within a distance SL^6 of it, is given by

$$P_6^8(0) = \sum_{k=0}^{L^D} P_7^8(k) [P_6^7(0)]^k. \quad (\text{B3})$$

Here we are adding a series of conditional probabilities. The term $P_7^8(k)[P_6^7(0)]^k$ is the probability that if the center of the EUV region simultaneously lies within k of the L^D substructures of hierarchy 7 [the expression $P_7^8(k)$], then no substructures of hierarchy 6, within those substructures of hierarchy 7, will be any closer than SL^6 to the center of the EUV region. Since $P_6^7(0)$ is independent of each of the k substructures of hierarchy 7, the expression $P_7^8(k)$ must be multiplied by $[P_6^7(0)]^k$. The choice of k out of L^D indistinguishable substructures means that the probability distribution for $P_7^8(k)$ is binomial. Thus,

$$P_7^8(k) = \binom{L^D}{k} (p)^k (1 - p)^{L^D - k}, \quad (\text{B4})$$

where p , the probability that the center of the EUV region is found *within* a substructure of hierarchy 7, is given by

$$p = \frac{(4/3)\pi(SL^7)^3}{(4/3)\pi(SL^8)^3} = L^{-3}. \quad (\text{B5})$$

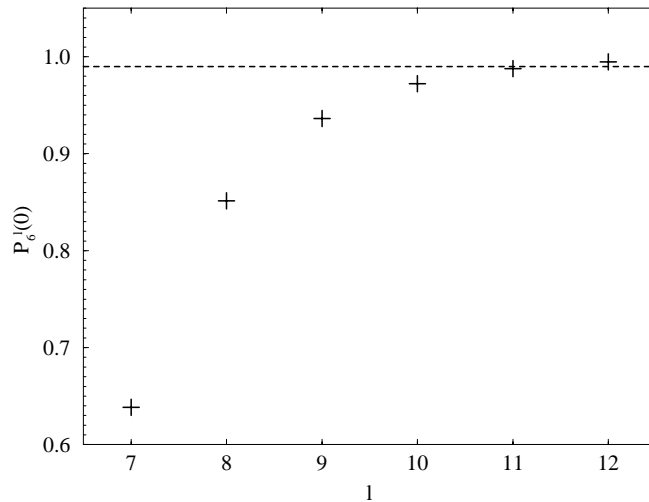


FIG. 6.— $P_6^l(0)$ as a function of l . $P_6^l(0) \approx 0.99$ (dashed line) when $l = 11$.

Combining equations (B3), (B4), and (B5) together gives

$$P_6^8(0) = \sum_{k=0}^{L^D} \binom{L^D}{k} [L^{-3} P_6^7(0)]^k (1 - L^{-3})^{L^D - k} = [P_6^7(0) L^{-3} + (1 - L^{-3})]^{L^D}. \quad (\text{B6})$$

Equation (B5) applies to all cases in which the substructure under consideration is one less than the fractal. This means equation (B6) is generalized by replacing the superscripts 7 and 8 with l and $l - 1$. This gives

$$P_6^l(0) = [L^{-3} P_6^{l-1}(0) + (1 - L^{-3})]^{L^D}, \quad (\text{B7})$$

establishing equation (46) in the text. Figure 6 shows a plot of $P_6^l(0)$ as a function of l for $L = 3.2098$ and $D = 2.3$. Note that when $l = 11$, we have $P_6^{11}(0)$ close to 0.99 (horizontal dashed line).

REFERENCES

- Baldwin, J. A., Ferland, G. J., Korista, K. T., & Verner, D. 1995, *ApJ*, 455, L119
- Blandford, R. D. 1990, in *Saas-Fee Advanced Course, Vol. 20, Active Galactic Nuclei*, ed. T. J.-L. Courvoisier & M. Mayor (Berlin: Springer), 161
- Blandford, R. D., & Payne, D. G. 1982, *MNRAS*, 199, 883
- Bottorff, M. C., & Ferland, G. J. 2000, *MNRAS*, 316, 103
- Collin-Souffrin, S. 1987, *MNRAS*, 179, 60
- Crenshaw, D. M., & Kraemer, S. B. 1999, *ApJ*, 521, 572
- Davidson, K., & Netzer, H. 1979, *Rev. Mod. Phys.*, 51, 715
- Elmegreen, B. G. 1997, *ApJ*, 477, 196
- . 1999, *ApJ*, 527, 266
- Elmegreen, B. G., & Falgarone, E. 1996, *ApJ*, 471, 816
- Ferland, G. J. 1999, in *ASP Conf. Ser. 162, Quasars and Cosmology*, ed. G. J. Ferland & J. A. Baldwin (San Francisco: ASP), 147
- George, I. M., Turner, T. J., Netzer, H., Nandra, K., Mushotzky, R. F., & Yaqoob, T. 1998, *ApJS*, 114, 73
- Heithausen, A., Bensch, F., Stutzki, J., & Falgarone, E. 1998, *A&A*, 331, L65
- Korista, K. T., Baldwin, J. A., Ferland, G. J., & Verner, D. 1997, *ApJS*, 108, 401
- Mac Low, M.-M., & Ossenkopf, V. 2000, *A&A*, 353, 339
- Marshall, H. H., et al. 1997, *ApJ*, 479, 222
- Mathews, W. G. 1983, *ApJ*, 272, 390
- . 1986, *ApJ*, 305, 187
- Mathur, S., Elvis, M., & Wilkes, B. 1999, *ApJ*, 519, 605
- Netzer, H. 1990, in *Saas-Fee Advanced Course, Vol. 20, Active Galactic Nuclei*, ed. T. J.-L. Courvoisier & M. Mayor (Berlin: Springer), 57
- Netzer, H., & Alexander, T. 1994, *MNRAS*, 270, 781
- Netzer, H., & Laor, A. 1993, *ApJ*, 404, L51
- Peterson, B. M. 1997, *An Introduction to Active Galactic Nuclei* (Cambridge: Cambridge Univ. Press)
- Rees, M. J. 1987, *MNRAS*, 228, 47
- Reynolds, C. S. 1997, *MNRAS*, 286, 513
- Reynolds, C. S., & Fabian, A. C. 1995, *MNRAS*, 273, 1167
- Woltjer, L. 1990, in *Saas-Fee Advanced Course, Vol. 20, Active Galactic Nuclei*, ed. T. J.-L. Courvoisier & M. Mayor (Berlin: Springer), 1
- Zheng, W., Kriss, G. A., Telfer, R. C., Grimes, J. P., & Davidsen, A. F. 1997, *ApJ*, 475, 469